

Non-circular semiconductor nanorings of type I and II: Emission kinetics in the exciton Aharonov-Bohm effect

Michal Grochol and Roland Zimmermann

Institut für Physik der Humboldt-Universität zu Berlin, Newtonstr. 15, 12489 Berlin, Germany

(Dated: October 27, 2018)

Transition energies and oscillator strengths of excitons in dependence on magnetic field are investigated in type I and II semiconductor nanorings. A slight deviation from circular (concentric) shape of the type II nanoring gives a better observability of the Aharonov-Bohm oscillations since the ground state is always optically active. Kinetic equations for the exciton occupation are solved with acoustic phonon scattering as the major relaxation process, and absorption and luminescence spectra are calculated showing deviations from equilibrium. The presence of a non-radiative exciton decay leads to a quenching of the integrated photoluminescence with magnetic field.

PACS numbers: 78.20.Bh, 71.35.Ji, 78.67.Hc, 71.35.Cc, 78.55.-m

I. INTRODUCTION

The Aharonov-Bohm effect (ABE) rests upon the action of the vector potential on quantum mechanical particles. The idea behind is quite simple: A charge particle orbiting around a region with non-zero magnetic flux $\Phi_B = \int \mathbf{B} \cdot d\mathbf{S}$ acquires an energy which is a periodic function of the magnetic flux Φ_B , the period being given by the magnetic flux quantum h/e . Shortly after its theoretical prediction,¹ the ABE has been observed experimentally.^{2,3} Doped semiconductor nanorings are among actual realizations⁴ where the ABE could be detected with high precision.

The exciton Aharonov-Bohm effect is a more recent invention: The neutral exciton consisting of electron and hole is predicted to show a similar oscillating behavior. Originally, a related many-body system has been studied by Wendler and coworkers^{5,6} who have considered the Coulomb effect when placing two electrons into a quantum ring – instead of electron and hole as in the present exciton case. They form a kind of Wigner molecule with interesting properties like crystallization. The approximations used originally allowed for an analytic solution of the ground state and the related persistent current. Later on, a full calculation was carried out, but always using a rigid lateral confinement in the ring.⁷

For the exciton Aharonov-Bohm effect (X-ABE), the limiting case of a nanoring with zero width has been studied first as well.^{8,9} The simplicity of the model allowed to investigate many aspects of X-ABE like the Berry phase and persistent current,¹⁰ absorption,¹¹ or deviation from circular symmetry due to the presence of impurities.^{12,13} One basic result was that the X-ABE can only be observed as long as the ring diameter is comparable or below the exciton Bohr radius a_B .⁹ Since the ring size cannot be made arbitrarily small, a better idea is to increase a_B , i.e. to weaken the exciton. This can be achieved by separating electron and hole using a static electric field,^{14,15} or going to type II material combinations where electron and hole are confined in different regions.^{12,13,16,17}

In the original ABE idea, the particle path was as-

sumed to lie in a region with zero magnetic field, which means to concentrate the magnetic flux into the middle of the ring. For a semiconductor nanoring of nanometer size, this is technically very demanding – if not impossible using state-of-the-art techniques. Therefore, for X-ABE a situation with the magnetic field penetrating homogeneously the nanoring is more realistic. Then, the energy in dependence on magnetic field acquires a non-oscillating part roughly proportional to B^2 as well which can complicate the extraction of X-ABE oscillations enormously.

First calculations for excitons in a *circular nanoring* with *finite width* and homogeneous penetrating magnetic field^{18,19,20} could not find the X-ABE for the ground state. Theoretical progress was made by calculations on two-dimensional annular lattices.²¹ X-ABE oscillations were found but the B^2 energy shift was not included. Our recent calculations for type I and II nanorings with finite width in Ref. 22 have clearly shown that the ground state energy has an oscillatory component, which is related to the exciton persistent current. For extracting its amplitude, we have proposed to calculate the second derivative of the energy with respect to B . On the search for optimal nanoring parameters, we have discussed in detail different material combinations for type II nanorings.

Compared to Ref. 22, the present work deals with *non-circular geometry* and gives a detailed study of *exciton kinetics* in order to calculate exciton occupation which is not necessarily in equilibrium with the lattice temperature. We restrict ourselves to incoherent and steady-state excitation following Ref. 23. A first attempt to calculate the exciton photoluminescence (PL) in zero width nanorings with a single impurity (and also quantum dots with respect to X-ABE) has been presented recently in Ref. 12. As a simplification, however, an equilibrium Maxwell-Boltzmann distribution for the excitons has been assumed, and only the integrated PL intensity was shown. We have started with a more realistic exciton kinetics, still in the zero width model for circular nanorings in Ref. 24. Non-radiative decay channels have been identified to be responsible for the decrease of the integrated PL signal with increasing magnetic field, which is

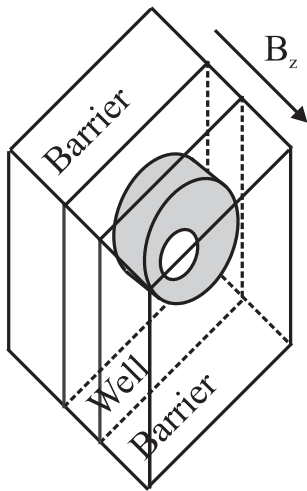


FIG. 1: Schematic drawing of the investigated non-circular (eccentric) nanoring (shaded) embedded in a quantum well

named PL quenching.

The experimental situation for the X-ABE is far from clear: An ensemble of InP/GaAs type II quantum *dots* has been studied in Ref. 25 and a theoretical explanation based on Ref. 26 indicated some X-ABE oscillations in a single dot. Later on, the non-circular shape of the quantum dot (D_1 and D_2 symmetry [see Section II]) has been taken into account.¹² Furthermore, in a recent single dot experiment²⁷ on InP/GaAs quantum dots (grown under different conditions) no oscillations have been observed. This is consistent with our recent calculation for embedded InP/GaAs quantum dots in Ref. 28. In a nanoring, only the ABE for negatively charged excitons – trions – has been observed.²⁹ The X-ABE in nanorings still waits

for its unambiguous experimental verification.

The paper is organized as follows. The exciton Hamiltonian is given in Section II in radial and angular variables, and its matrix elements are analyzed according to the ring symmetry using arguments of group theory. Examples for energies, oscillator strengths, and oscillation amplitudes of the X-ABE are shown in Section III, for both type I and type II structures. Kinetic equations for the exciton occupation including acoustic phonon scattering and several decay channels are discussed in Section IV. Its numerical solution allows to plot absorption and photoluminescence spectra for various parameters (Section V). The paper is concluded in Section VI, while more technical details are deferred to the Appendix.

II. EXCITON HAMILTONIAN

For the heavy-hole exciton in nanostructures, effective mass theory with appropriate in-plane (m_a) and growth direction masses ($m_{a,z}$) is used often. The subscript denotes electron ($a = e$) and hole quantities ($a = h$). Within this approximation, we will investigate a structure which consists of a narrow quantum well with confining potentials $U_a(z_a)$ into which a nanoring of general symmetry is embedded. The corresponding lateral confinement is given by $V_a(\mathbf{r}_a)$. The three-dimensional vector \mathbf{r} is decomposed into its two-dimensional in-plane part and the z -component in growth direction, $\mathbf{r}_a = (\mathbf{r}_a, z_a)$. The ring structure is schematically plotted in Fig. 1. Including a constant B -field in z -direction (perpendicular to the quantum well), we have the single exciton Hamiltonian

$$\hat{H} = \sum_{a=e,h} \left(\frac{1}{2m_a} (\hat{\mathbf{p}}_{\mathbf{r}_a} \mp e\mathbf{A}(\mathbf{r}_a))^2 + \frac{1}{2m_{a,z}} \hat{p}_{z_a}^2 + U_a(z_a) + V_a(\mathbf{r}_a) \pm g_a^* \mu_B B \sigma_a^z \right) - \frac{e^2}{4\pi\epsilon_0\epsilon_S |\mathbf{r}_e - \mathbf{r}_h|}, \quad (1)$$

where upper (lower) sign refer to electron (hole). g_a^* are effective g factors, $\mu_B = e\hbar/2m_0$ is the Bohr magneton, and σ_a^z the Pauli spin matrix (along z). The vector potential is used in symmetric gauge, $\mathbf{A}(\mathbf{r}) = \frac{1}{2}\mathbf{B} \times \mathbf{r}$. The Coulomb potential between electron and hole (last term) is screened by the static dielectric constant ϵ_S of the semiconductor material.

Angular momentum and spin parts of the wave function can be separated for the heavy-hole exciton, forming a quadruplet with the z -projection of the total angular momentum $M = \pm 1$ (optically active or bright states, with circular polarization σ^\pm) and $M = \pm 2$ (dark states). Combining electron and hole g factors into effective exciton g factors^{30,31} as $g_{X,\pm 1}^* = \pm(g_h^* + g_e^*)$ and

$g_{X,\pm 2}^* = \pm(g_h^* - g_e^*)$ allows to write the spin-dependent contribution to the exciton energy as

$$E_M^{spin} = \frac{1}{2} g_{X,M}^* \mu_B B, \quad (2)$$

which gives rise to the Zeeman splitting linear in B . In the following this spin contribution is not written explicitly since its addition to the exciton energies is straightforward. The exciton exchange interaction gives rise to an additional fine structure splitting which is neglected here in view of the dominant B -field effects.

Due to the confinement strength in z -direction, we factorize from the total wave function the product of sub-level wave functions³² of the lowest electron and hole

states in the quantum well. The remaining in-plane part of the wave function has to be calculated from the z -averaged Hamiltonian.²² Introducing polar coordinates and difference and sum angle [$\phi = \phi_e - \phi_h$, $\Phi = (\phi_e + \phi_h)/2$], we arrive at

$$\begin{aligned} \hat{H} = & \sum_{a=e,h} \left[-\frac{\hbar^2}{2m_a} \frac{1}{r_a} \frac{\partial}{\partial r_a} \left(r_a \frac{\partial}{\partial r_a} \right) \right. \\ & + \frac{1}{2m_a r_a^2} \left(i\hbar \left[\frac{\partial}{\partial \phi} \pm \frac{1}{2} \frac{\partial}{\partial \Phi} \right] - \frac{eB}{2} r_a^2 \right)^2 \\ & \left. + V_a(r_a, \Phi \pm \frac{1}{2}\phi) \right] - V_C(r_e, r_h, \phi), \end{aligned} \quad (3)$$

where $+$ ($-$) sign refers to electron (hole). The confinement averaged Coulomb potential $V_C(r_e, r_h, \phi)$ has been defined in Ref. 22.

The exciton eigenfunction of the state α as solution of

$$\hat{H}\Psi_\alpha = E_\alpha\Psi_\alpha \quad (4)$$

is expanded into the basis of angular momentum eigenfunctions,

$$\Psi_\alpha(r_e, r_h, \phi, \Phi) = \frac{1}{2\pi} \sum_{l,L} u_{l,L,\alpha}(r_e, r_h) e^{il\phi} e^{iL\Phi}. \quad (5)$$

The azimuthal boundary conditions have the usual form

$$\begin{aligned} \Psi_\alpha(r_e, r_h, \phi_e, \phi_h) &= \Psi_\alpha(r_e, r_h, \phi_e + 2\pi, \phi_h), \\ \Psi_\alpha(r_e, r_h, \phi_e, \phi_h) &= \Psi_\alpha(r_e, r_h, \phi_e, \phi_h + 2\pi), \end{aligned} \quad (6)$$

which leads using Eq. (5) to the following relation between l and L :

$$L \text{ even: } l \text{ integer; } \quad L \text{ odd: } l \text{ half integer.} \quad (7)$$

The expansion functions $u_{l,L,\alpha}(r_e, r_h)$ obey a coupled system of Schrödinger equations. The confining potential produces the matrix elements

$$\begin{aligned} \langle lL|V_a(r_a, \phi_a)|l'L'\rangle &= \delta_{l-l', \pm \frac{L-L'}{2}} V_{L-L'}^a(r_a), \\ V_k^a(r_a) &= \frac{1}{2\pi} \int_0^{2\pi} d\phi_a V_a(r_a, \phi_a) e^{ik\phi_a}, \end{aligned} \quad (8)$$

where again $+$ ($-$) sign corresponds to the electron (hole). From the reality of $V_a(r_a, \phi_a)$ follows $V_k^a = (V_{-k}^a)^*$.

The confining potential can have an arbitrary symmetry (see Fig. 2 for examples) which is classified by the two-dimensional point group. There are two types: (i) C_n which consists of all rotations about the origin by multiples of the angle $2\pi/n$ and (ii) D_n which adds to the rotations of C_n reflections with respect to n axes passing through the origin. Within C_n , the potential $V_a(r_a, \phi_a)$ is invariant under rotations by multiples of the angle $2\pi/n$. Changing the integration variable in Eq. (8) by $\phi'_a = \phi_a + 2\pi/n$ we obtain

$$V_k^a(r_a) = \frac{1}{2\pi} \int_0^{2\pi} d\phi_a V_a(r_a, \phi_a) e^{ik(\phi_a + \frac{2\pi}{n})}. \quad (9)$$

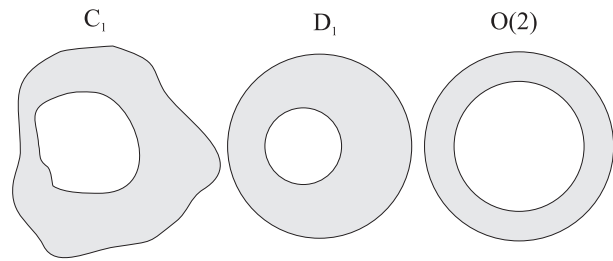


FIG. 2: Schematic picture of nanorings with different symmetries.

TABLE I: The symmetry of the ring geometry leads to restrictions for the matrix elements of the in-plane potential Eq. (8).

| Point group of the ring | Non-zero elements of V_k^a at |
|-------------------------|--|
| C_n | $k = jn$ (j integer) |
| D_n | $k = jn$ (j integer) and $V_k^a = V_{-k}^a$ |
| $O(2)$ | $k = 0$ |

Comparison with Eq. (8) shows that only elements with $k = jn$ (j integer) can be non-zero. Using similar arguments the reflections in D_n imply $V_k^a = V_{-k}^a$ to hold. The symmetry properties are summarized in Tab. I.

In the absence of any symmetry (C_1) all matrix elements in Eq. (8) can be non-zero. For increased symmetry (C_n or D_n , $n > 1$) the matrix decomposes into n block matrices, since the matrix elements $\langle lL|V_a|l'L'\rangle$ are non-zero only if $L-L' = n$. In the limiting case of large n the point groups C_n and D_n converge to the point group of the circle $O(2)$. Due to the rotational invariance of the circle, one degree of freedom can be factorized. This is the total angular motion since the corresponding commutator with the Hamiltonian vanishes, $[\hat{H}, -i\hbar\partial/\partial\Phi] = 0$.

The Coulomb potential $V_C(r_e, r_h, \phi)$ depends only on the relative angle, and its matrix elements are diagonal in L

$$\langle lL|V_C(r_e, r_h, \phi)|l'L'\rangle = \delta_{LL'} V_k^C(r_e, r_h), \quad (10)$$

$$V_k^C(r_e, r_h) = \frac{1}{2\pi} \int_0^{2\pi} d\phi V_C(r_e, r_h, \phi) \cos(k\phi).$$

Putting all terms together, the matrix elements of the Hamiltonian are given by

$$\begin{aligned} \langle lL|\hat{H}(r_e, r_h, \phi, \Phi)|l'L'\rangle = & \quad (11) \\ & \delta_{ll'} \delta_{LL'} \sum_{a=e,h} \left[\frac{\hbar^2}{2m_a} \left\{ -\frac{1}{r_a} \frac{\partial}{\partial r_a} \left(r_a \frac{\partial}{\partial r_a} \right) \right. \right. \\ & \left. \left. + \frac{1}{r_a^2} \left(l \pm \frac{L}{2} + \frac{eB}{2\hbar} r_a^2 \right)^2 \right\} \right] - \delta_{LL'} V_{l-l'}^C(r_e, r_h) \\ & + \delta_{l-l', \frac{L-L'}{2}} V_{L-L'}^e(r_e) + \delta_{l'-l, \frac{L-L'}{2}} V_{L-L'}^h(r_h). \end{aligned}$$

The azimuthal kinetic terms can be rewritten as

$$\begin{aligned} \sum_{a=e,h} \frac{\hbar^2}{2m_a r_a^2} \left(l \pm \frac{L}{2} + \frac{eB}{2\hbar} r_a^2 \right)^2 = \\ \frac{\hbar^2}{2\mu_X r_X^2} \left(l + \frac{eB}{2\hbar} r_X^2 + \frac{L}{2} p \right)^2 \\ + \frac{\hbar^2}{2(m_e r_e^2 + m_h r_h^2)} \left(\frac{eB}{2\hbar} (r_e^2 - r_h^2) + L \right)^2 \end{aligned} \quad (12)$$

with the exciton reduced mass $\mu_X = m_e m_h / (m_e + m_h)$. Further, r_X is an effective ring radius for the exciton and p a phase shift, defined as

$$r_X^2 = \frac{r_e^2 r_h^2 (m_e + m_h)}{m_e r_e^2 + m_h r_h^2}, \quad p = \frac{m_h r_h^2 - m_e r_e^2}{m_h r_h^2 + m_e r_e^2}. \quad (13)$$

Equation (12) resembles the zero-width ring model discussed in Ref. 22. For $L = 0$, the last line is responsible for the overall increase of energies quadratically in B , while the second line is the source of the X-ABE oscillations. We will use Eq. (12) in Section III for extracting a reasonable estimate of the B oscillation period.

For dipole-allowed optical interband transitions, the oscillator strength f_α of the exciton state α is given by the amplitude of finding electron and hole at the same place,³³

$$f_\alpha = d_{cv} \int dr \Phi_\alpha(r, r), \quad (14)$$

where d_{cv} is the interband dipole matrix element. Introducing the single sublevel approximation and the expansion Eq. (5), we find

$$f_\alpha = d_{cv} \sum_l \int_0^\infty dr r u_{l,0,\alpha}(r, r). \quad (15)$$

Only the wave function component with $L = 0$ contributes to the oscillator strength. States with non-zero oscillator strength are called bright states, while dark states have $f_\alpha = 0$.

As an example of a structure with low symmetry, we investigate a ring with D_1 symmetry. Our simple model has two circles as boundaries. The inner one is centered at the origin (radius r_1), while the outer one (radius r_2) is displaced by b , as indicated in Fig. 3. Electron energy spectra have been investigated for such a structure in Ref. 34, calling the ring *eccentric*. We will use in what follows non-circular and eccentric as equivalent names, contrasting to *concentric* and circular. The potential is assumed to be constant with a value V_0^a between these two rings, and set to zero outside. In the figures, however, zero of energy is set to the confinement gap of the quantum well made from the ring material.

The matrix element Eq. (8) reduces to

$$\begin{aligned} V_k^a(r_a) = \frac{V_0^a}{2\pi} \int_{-\pi}^{\pi} d\phi e^{ik\phi} \theta(r_a - r_1) \times \\ \theta(r_2^2 - (r_a \cos(\phi) - b)^2 - r_a^2 \sin^2(\phi)). \end{aligned} \quad (16)$$

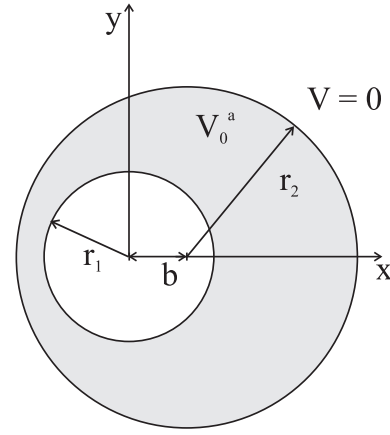


FIG. 3: Schematic picture of a nanoring with D_1 symmetry. Within the gray region, the potential is nonzero. Inner and outer ring boundaries are circles with radii r_1 and r_2 , the centers of which are displaced by b .

The unit step functions determine the integration boundaries to be $\pm\pi$ or $\pm\phi(r_a)$ where

$$\cos(\phi(r_a)) = \frac{1}{2} \frac{b^2 + r_a^2 - r_2^2}{r_a b}. \quad (17)$$

The result can be given analytically,

$$\begin{aligned} V_k^a(r_a) = V_0^a \left[\delta_{k,0} \theta(r_a - r_1) \theta(r_2 - b - r_a) \right. \\ \left. + \frac{1}{k\pi} \sin(k\phi(r_a)) \theta(r_a - r_2 + b) \theta(r_2 + b - r_a) \right], \end{aligned} \quad (18)$$

which properly satisfies the relation $V_k^a = V_{-k}^a$ inherent to D_1 symmetry.

The circular ring is contained as a special case: Setting $b = 0$, only the first line in Eq. (18) contributes,

$$V_k^a(r_a) = V_0^a \delta_{k,0} \theta(r_2 - r_a) \theta(r_a - r_1). \quad (19)$$

Consequently, the Hamiltonian matrix is fully diagonal in L , and the wave function expansion Eq. (5) reduces to the sum over l , while $L = L_\alpha$ is fixed and therefore a good quantum number.

III. X-ABE OF THE EXCITON GROUND STATE

We begin with a discussion of the X-ABE for the exciton ground state in concentric and eccentric nanorings of type I and II as schematically plotted in Fig. 4. The material parameters used are summarized in Tab. II. The effective masses are chosen according to the material in which the particle is found predominantly. The values of the mass density, the sound velocity, and the deformation potentials are taken for the ring material.

In the calculation, B -field strengths up to $B = 25$ T are used which can be easily achieved in experiment. The radial coordinates in Eq. (11) have been discretized on a

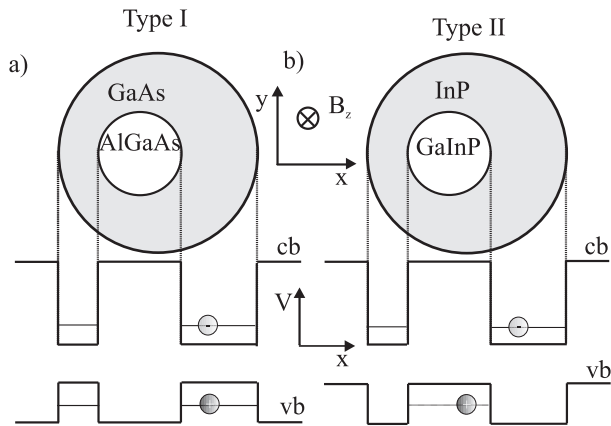


FIG. 4: Schematic view of in-plane geometry (top) and energy profiles for conduction and valence band (bottom) for the investigated nanorings of type I a) and type II b). Specific electron and hole positions are visualized.

TABLE II: Confinement potentials V_0^a , static dielectric constant ϵ_S , in-plane effective masses m_a , g factors g_a^* , mass density ρ_M , sound velocity s , and deformation potentials for conduction (D_c) and valence band (D_v).

| | GaAs/Al _{0.23} Ga _{0.77} As | InP/Ga _{0.51} In _{0.49} P |
|--------------------------------|---|---|
| V_0^e (meV) | -257 ^c | -600 ^b |
| V_0^h (meV) | -110 ^c | 50 ^b |
| ϵ_S | 12.5 ^a | 12.6 ^b |
| m_e/m_0 | 0.067 ^a | 0.077 ^b |
| m_h/m_0 | 0.36 ^a | 0.6 ^d |
| g_e^* | 0.1 ^g | 1.6 ^h |
| g_h^* | -1.2 ^g | -3.0 ^h |
| ρ_M (kg m ⁻³) | 5370 ^f | 4810 ^e |
| s (m/s) | 5330 ^f | 5230 ^e |
| D_c (eV) | 7.0 ^f | 6.0 ^c |
| D_v (eV) | -3.5 ^f | -0.6 ^c |

^aRef. 35.

^bRef. 36.

^cRef. 37.

^dRef. 38.

^eRef. 39.

^fRef. 35.

^gRef. 30.

^hRef. 40.

grid of 40 points with a grid step of 0.5 nm. The expansion of the wave function into l and L components has been checked for convergency of the results, leading to a truncation of $|l| < 13$ and $|L| < 10$. The subsequent numerical diagonalization was performed with the improved Lanczos method⁴¹ and checked with the Leapfrog method.^{42,43}

A. Type I nanoring

First, a nanoring of GaAs embedded in the surrounding material Al_{0.23}Ga_{0.77}As is considered. This type I structure has a confinement of both electron and hole within the nanoring.

The dependence of the lowest three exciton energies on magnetic field is plotted in Fig. 5a. In the case of circular symmetry ($b = 0$ nm, black curves) the states can be sorted according to their quantum number L_α . The ground state has $L_\alpha = 0$ (solid), the first and the second excited ones $L_\alpha = 1$ (dashed) and $L_\alpha = -1$ (dotted), respectively. The energies of the first excited states are degenerate at $B = 0$ T. This degeneracy is lifted at $B \neq 0$ with a relatively small splitting since the effective radial distance between electron and hole is small. In order to see this dependence more clearly, let us look upon Eq. (12). Due to the strong radial confinement, the coordinates r_a in Eq. (12) can be replaced by their expectation values $R_a = \langle r_a \rangle$. Their values being rather close in the present case ($R_e = 8.0$ nm, $R_h = 7.8$ nm), we realize that $L = \pm 1$ gives only a minor difference in the energy.

The case of non-circular symmetry ($b = 1$ nm, red (grey) curves in Fig. 5a) is qualitatively not different from the circular one since the energetically lowest states for different quantum numbers L do not cross. Their mixing leads to a larger splitting among states and lifts the degeneracy at $B = 0$ T. More important are the changes in the oscillator strength (Fig. 5b). The D_1 symmetry of the eccentric nanoring implies that there is one symmetry axis, let us say the x -axis, with reflection operator \hat{T}_x . The wave function transforms in the following way

$$\begin{aligned} \hat{T}_x \Psi_\alpha(x_e, y_e, x_h, y_h) &\equiv \Psi_\alpha(x_e, -y_e, x_h, -y_h) \\ &= \pm \Psi_\alpha(x_e, y_e, x_h, y_h). \end{aligned} \quad (20)$$

With respect to this symmetry operation, all states can be grouped into even and odd ones. The odd states have zero oscillator strength which follows immediately from Eq. (20). The doubly degenerate states of the concentric nanoring at $B = 0$ T can form an even and odd linear combination with respect to \hat{T}_x . As the symmetry is lowered these combinations get mixed. The energetic order of even and odd states can be estimated for the lowest ones. The ground state is always even as shown in Fig. 5b. The first excited is odd since the contribution of the Coulomb interaction is still large as in the ground state, while the kinetic energy is lower than for the next even state. Further excited states have different Coulomb contributions and that is why their order cannot be determined in general.

All lines in Fig. 5a seem to shift upwards quadratically in B , which is indeed the dominant part of the diamagnetic shift. In order to extract the tiny amplitude of the X-ABE oscillations, we have proposed in our previous publication Ref. 22 to calculate the second derivative of the exciton energy with respect to the B -field. This is shown in Fig. 5c.

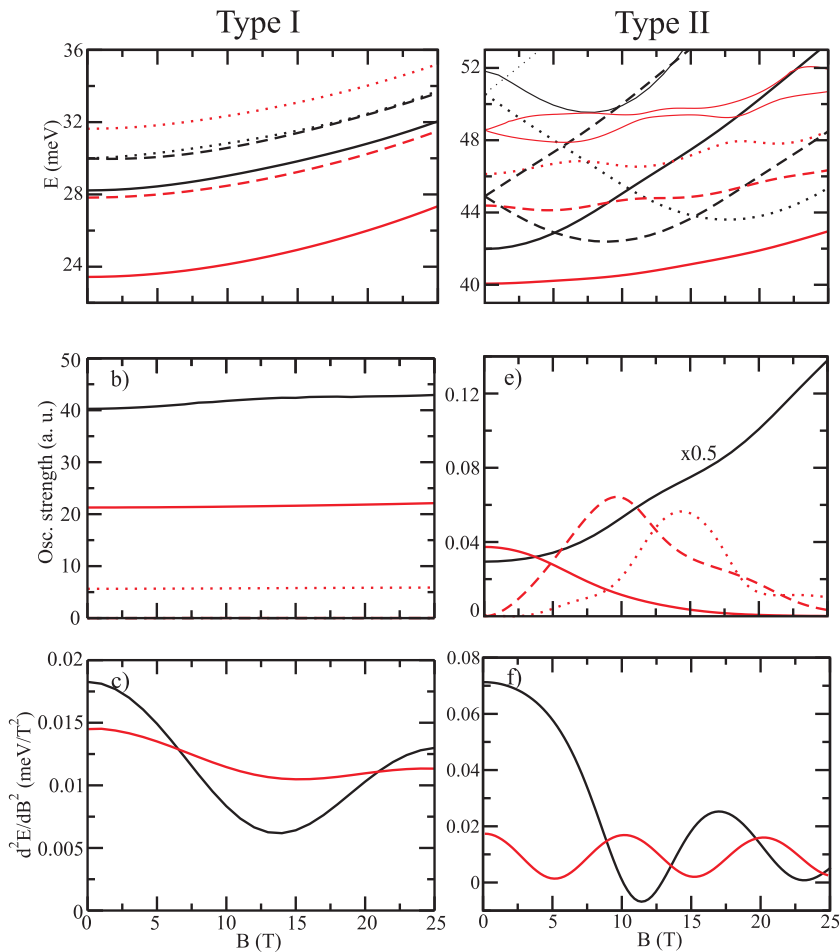


FIG. 5: (Color online) Calculated exciton properties in nanorings in dependence on magnetic field. The left column refers to a type I system (GaAs/AlGaAs) with ring radii $r_1 = 4$ nm, $r_2 = 12$ nm, while for the right column a type II system (InP/GaInP) with $r_1 = 8$ nm and $r_2 = 16$ nm has been considered. Results for a circular ring ($b = 0$) are shown in black, while red (grey) curves are obtained for a non-circular ring (type I: $b = 1$ nm, type II: $b = 0.5$ nm). The lowest exciton levels are shown in a) and d) (for details see text). The spin-dependent Zeeman energy is not included. In b) and c) the corresponding oscillator strengths f_α^2 are plotted. The lowest panel c) and d) show the second derivative of the ground state energy which quantifies the X-ABE oscillations.

The period can be estimated from the second line of Eq. (12), assuming that due to the confinement both $\langle r_e \rangle$ and $\langle r_h \rangle$ are almost constant, as

$$B_P = \frac{2\hbar}{e} \frac{1}{R_X^2}, \quad (21)$$

which is $B_P = 20.6$ T in the present case. The minima of the oscillatory component of the energy are found at $B = jB_P$, j being integer, and maxima at $B = jB_P/2$. Consequently, the minimum of the second derivative is found at around half of the oscillation period in all cases ($B_P/2 = 10.3$ T).

The oscillation amplitude is reduced for the eccentric nanoring. Here, the non-uniform ring width tends to push the exciton wave function into the broader part, thus weakening its ring topology which is a necessary ingredient for X-ABE oscillations. Note that for $b \geq r_2 - r_1$ the confinement potential reduces to a banana-shaped

quantum dot, and the ring topology is lost completely.

B. Type II nanoring

Secondly, we investigate a type II nanoring consisting of InP in the ring and $\text{Ga}_{0.51}\text{In}_{0.49}\text{P}$ outside, embedded into an AlAs barrier along z . Strain effects are taken into account only in so far as the hole is always found inside, $r_h < r_1$. A full inclusion of strain would modify the exact potential profile but not the $O(2)$ or D_1 symmetry.

For the concentric type II ring, Fig. 5d illustrates the crossings among states with different quantum number L_α (black solid $L_\alpha = 0$, dashed $L_\alpha = \pm 1$, and dotted $L_\alpha = \pm 2$). This crossing resembles more the ABE for individual carriers and can be traced back to the much reduced exciton effect in the present type II nanoring. In order not to overload Fig. 5d, some higher states have

been omitted. If the symmetry is reduced to D_1 (red [grey] curves), all states are mixed similar to the type I nanoring. Consequently, all crossings become anti-crossings and the energy dependence on the magnetic field differs not much from the type I nanoring, with reduced X-ABE oscillations (Fig. 5f).

The difference between type I and II nanorings becomes apparent when the oscillator strength is studied as depicted in Fig. 5e. The oscillator strength corresponding to different exciton states changes with the magnetic field as the character of the exciton wave function changes itself: The main component of the ground state wave function is $L = 0$ at $B = 0$ T and shifts to $L = 1$ at $B = 10$ T. This results in a decrease of the oscillator strength which is transferred to the first excited state (and increased due to the larger electron-hole overlap). Later on it is transferred to the second and higher excited states where different quantum numbers L mix strongly. Even though there is not any strict rule for the oscillator strength conservation, Fig. 5e suggests that it is approximately valid for the lowest exciton states. The rapid decay of the ground state oscillator strength with increasing magnetic field has interesting implications for the exciton kinetics (Section IV).

Unlike the type I nanoring, the oscillation period changes with b (Fig. 5f). This is also accompanied by a decrease of the oscillation amplitude due to the loss of the ring topology with increasing b . The oscillation period is now determined by the periodic change of the ground state main component from L to $L + 1$, thus by the center-of-mass motion. The exciton relative motion with the period B_P in Eq. (21) plays only a minor role for *every* value of $b \neq 0$. The value of the center-of-mass period can be estimated from the last term of Eq. (12) assuming again strong radial confinement,

$$B_{P,2} = \frac{2\hbar}{e} \frac{1}{R_e^2 - R_h^2}. \quad (22)$$

In the present case, taking $R_e = \langle r_e \rangle = 12.3$ nm and $R_h = \langle r_h \rangle = 4.4$ nm we obtain $B_{P,2} = 9.9$ T, which agrees well with the observed period in Fig. 5f.

In Fig. 6 correlated one-particle densities are plotted. They are defined as conditional probability to find a particle, either electron or hole, in the exciton while fixing the coordinates of the other particle at a certain position marked by a large dot. For the formal definition, see Eqs. (A1, A2). This concept has been used also for analyzing the two-electron Wigner molecule in a quantum dot.⁷ An inspection of Fig. 6 reveals how the loss of the circular symmetry in the eccentric nanoring modifies the wave function. By fixing the hole position at the right (wide) side of the ring, most of the electron density is found there as well (Fig. 6a), which resembles the situation in a concentric ring (not shown). The same is true for the hole (Fig. 6c). On the other hand, by fixing either the electron or the hole on the opposite narrow side of the ring, the picture changes. Due to the strength of the ring confinement and the weakness of the Coulomb in-

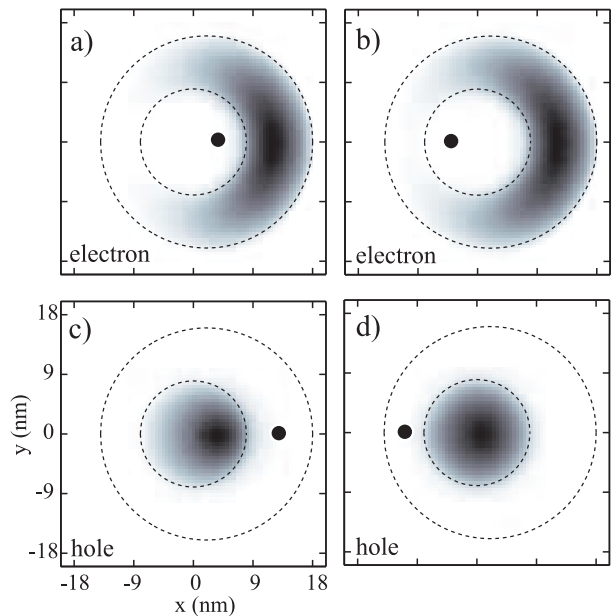


FIG. 6: Correlated electron and hole densities of the exciton ground state at zero magnetic field for a non-circular type II nanoring (InP/GaInP, $r_1 = 8$ nm, $r_2 = 16$ nm, $b = 2$ nm). The black dot indicates the chosen coordinates of the other particle.

teraction in type II structures, the electron is still found on the right where the confinement energy is minimal (Fig. 6b). Since the electron density is very small on the opposite side, the Coulomb correlation seen by the hole is tiny, and an almost circular – i.e. one-particle like – hole density is found in Fig. 6d.

Finally, let us briefly consider the case of a free electron-hole pair which has been investigated for type I nanorings in Ref. 34. Formally, we switch off the Coulomb interaction V_C in the Hamiltonian Eq.(1). The free electron-hole transitions shown as dashed curves in Fig. 7a are dominated by the electron level since the hole part refers to an almost fixed angular quantum number due to the small effective hole radius of 4 nm. Therefore, the first levels can be characterized by the electron quantum numbers $l_e = 0, -1, +1$. Their degeneracy at zero magnetic field is lifted when switching on the Coulomb interaction (solid curves), similarly to Fig. 5d. The overall down shift in energy is a measure of the exciton binding energy.

The second derivative displayed in Fig. 7b shows that the diamagnetic shift (being proportional to the relative distance) of the free electron-hole pair is larger than in the exciton. The reason is the Coulomb attraction in the exciton which brings electron and hole closer together. The oscillation amplitude, however, is getting stronger for the exciton. We conclude that the ring topology of the electron part is stabilized due to the Coulomb attraction with the hole. Therefore, surprisingly in the specific type II example, the ring eccentricity is felt not as strong for the exciton compared with the free e-h- pair.

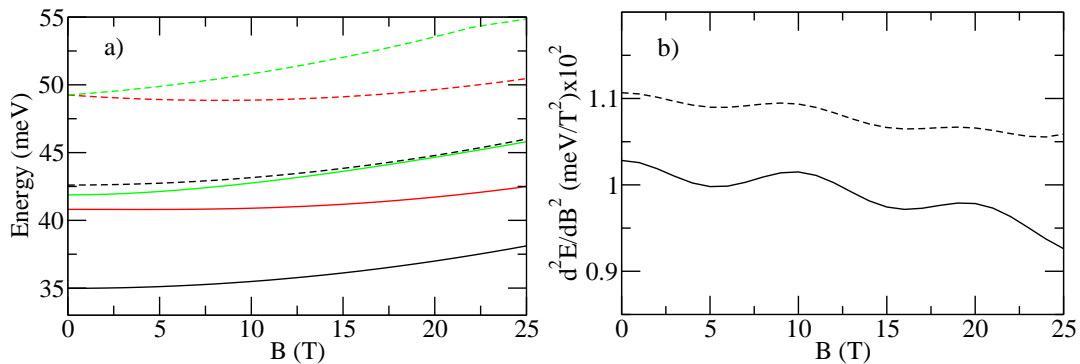


FIG. 7: (Color online) Calculated exciton (solid) and free electron-hole pair (dashed) properties in non-circular nanorings of type II (InP/GaInP) with $r_1 = 8$ nm, $r_2 = 16$ nm, and $b = 2$ nm as a function of magnetic field. The ground state in black, the first and the second excited state in red (dark grey) and green (light grey) are shown in a) (the spin-dependent Zeeman energy is not included). In b) the second derivative of the ground state energy is depicted.

To summarize this section, we have demonstrated that the amplitude of X-ABE weakens when going from circular to non-circular symmetry since the wave function tends to lose its ring topology. However, if the asymmetry is weak and electron and hole are spatially separated as in type II structures, the ground state still exhibits oscillations in its energy, while being always bright and observable by optical means.

IV. KINETIC EQUATIONS

For calculating the photoluminescence emitted from the nanoring, we need to know the occupation N_α of each exciton states. For the linear density regime and incoherent excitation, the relevant set of kinetic equations has been derived in Ref. 23,

$$\frac{dN_\alpha}{dt} = g_\alpha + \sum_\beta \gamma_{\alpha\beta} N_\beta - (r_\alpha + d_\alpha + \sum_\beta \gamma_{\beta\alpha}) N_\alpha. \quad (23)$$

Here, g_α is a state dependent generation term which stands for the last term in a chain of optical phonon emission events after optical interband excitation.³⁵ The radiative decay rate r_α of a localized exciton state contains emission into both TE and TM polarization and is found proportional to the squared oscillator strength,⁴⁴

$$r_\alpha = \frac{4}{3} \frac{E_g^3 n_R}{\hbar^4 c^3} |f_\alpha|^2, \quad (24)$$

where n_R is the refractive index and E_g the band gap. In Eq. (23), d_α is a phenomenological non-radiative decay rate, representing processes as e. g. exciton annihilation via impurities, escape into the wetting layer, or Auger processes. These processes are not treated explicitly in the present theory.

The acoustic phonon scattering rates $\gamma_{\alpha\beta}$ are defined

as

$$\gamma_{\alpha\beta} = \frac{2\pi}{\hbar} \sum_{\mathbf{q}} |t_{\alpha\beta}^{\mathbf{q}}|^2 [(n_B(\hbar\omega_{\mathbf{q}}) + 1)\delta(E_\beta - E_\alpha - \hbar\omega_{\mathbf{q}}) + n_B(\hbar\omega_{\mathbf{q}})\delta(E_\beta - E_\alpha + \hbar\omega_{\mathbf{q}})] \quad (25)$$

where $n_B(\hbar\omega_{\mathbf{q}})$ is the Bose-Einstein distribution of acoustic phonons with dispersion $\hbar\omega_{\mathbf{q}} = \hbar s q$ (s – sound velocity). They obey the relation of detailed balance between in- and out scattering of a given state,

$$\gamma_{\beta\alpha} = \gamma_{\alpha\beta} e^{(E_\alpha - E_\beta)/k_B T}, \quad (26)$$

with the phonon (i.e. lattice) temperature T . Strictly speaking, lattice vibrations in nanostructures differ from the respective bulk ones,⁴⁵ but for the present purpose this refinement is of minor importance.⁴⁶ The evaluation of the exciton-phonon matrix elements $t_{\alpha\beta}^{\mathbf{q}}$ for deformation potential scattering is given in the Appendix.

In the exciton scattering with acoustic phonons we have taken into account only the spin diagonal part. Indeed, there is non-diagonal scattering (“spin-flip”) as well due to the lack of the inversion symmetry in nanostructures – Rashba effect.⁴⁷ Under linearly polarized excitation, the initial generation g_α is spin independent. Assuming that in the final stage of thermalization spin-flip processes can be neglected, we expect an equal occupation of spin up and down bright states. This is supported by recent experiments showing almost no difference in intensities between σ^+ and σ^- polarized lines.⁴⁸

The kinetic equations are solved numerically for the steady state situation $dN_\alpha/dt = 0$. The resulting occupations N_α enter the photoluminescence spectrum $I(E)$,

$$I(E) = \sum_{\alpha} r_{\alpha} N_{\alpha} \delta(E - E_{\alpha}). \quad (27)$$

Note that the linear absorption spectrum $D(E)$ does not depend on the occupations,

$$D(E) = \sum_{\alpha} r_{\alpha} \delta(E - E_{\alpha}). \quad (28)$$

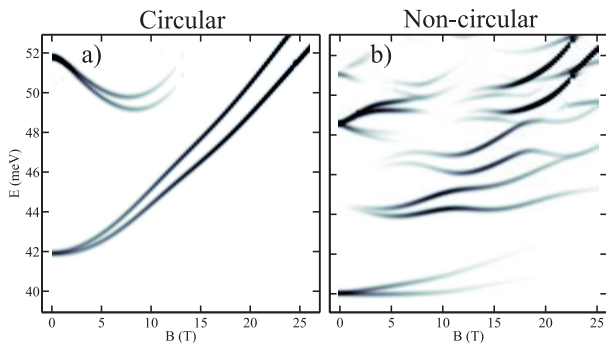


FIG. 8: Calculated absorption spectra of a circular ($b = 0$ nm) and non-circular ($b = 0.5$ nm) type II nanoring (InP/GaInP, $r_1 = 8$ nm, $r_2 = 16$ nm) including the spin contribution Eq. (2). All spectra are Gauss broadened with variance $\sigma = 0.1$ meV and displayed using a linear gray scale.

Again, a constant prefactor has been omitted.

Summing Eq. (23) over all states α , the phonon scattering terms cancel, and the following conservation law for the total pump rate P is found

$$P \equiv \sum_{\alpha} g_{\alpha} = \sum_{\alpha} (r_{\alpha} + d_{\alpha}) N_{\alpha}. \quad (29)$$

We will exploit this relation in Section V in the discussion of PL quenching. i.e. a decrease of the PL intensity with B -field.

V. ABSORPTION AND PHOTOLUMINESCENCE

Since in type I nanorings, the exciton energies and oscillator strengths do not depend much on the magnetic field, interesting effects like PL quenching are not to be expected. Therefore, we focus here on a type II system and investigate InP/GaInP nanorings with radii $r_1 = 8$ nm, $r_2 = 16$ nm. Results for an eccentric nanoring (c) are compared with a slightly eccentric one (n), having a center displacement b of 0.5 nm as used in Fig. 5, right panel. The radiative rates of the lowest state $\alpha = 0$ are rather small ($r_0^c = 0.042$ ns $^{-1}$ and $r_0^n = 0.027$ ns $^{-1}$ at $B = 0$ T) due to the tiny overlap between electron and hole in the wave function, as specific for any type II structure. Similar small radiative rates have been calculated for spatially indirect excitons in coupled quantum wells.⁴⁹ The exciton-phonon scattering rates from the first excited state down to the ground state are $\gamma_{01}^c = 102$ ns $^{-1}$ and $\gamma_{01}^n = 138$ ns $^{-1}$ at $B = 0$ T. These numbers clearly indicate that the exciton-phonon scattering dominates the kinetics.

The absorption spectra of the circular and non-circular nanorings plotted in Fig. 8 are calculated for linearly polarized light where both spin components Eq. (2) with $M = \pm 1$ are present. Therefore, all lines appear as Zeeman splitted doublets.

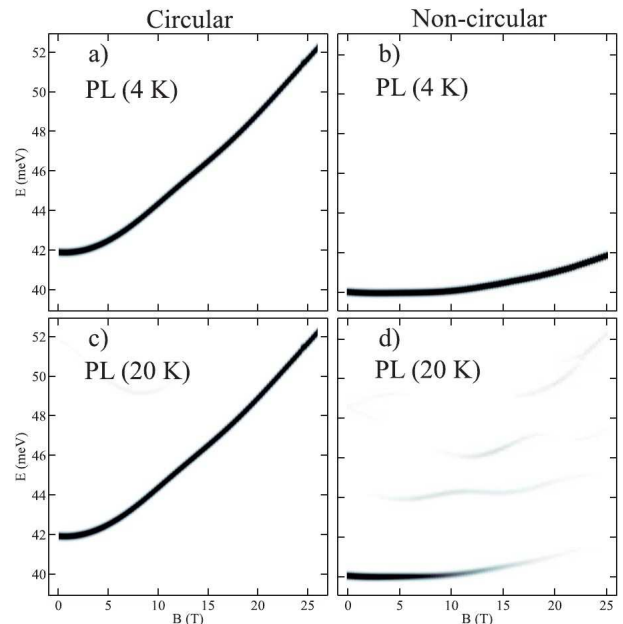


FIG. 9: Calculated photoluminescence spectra of a circular (a and c) and a non-circular (b and d) type II nanoring as in Fig. 8. Exciton occupations are calculated from the kinetic equation Eq. (23), fixing the phonon temperatures as indicated. Without non-radiative decay, $d_{\alpha} = 0$.

The absorption spectra plotted in Fig. 8 show pronounced differences between both nanorings: In the concentric nanoring only two doublets having quantum number $L_{\alpha} = 0$ are visible (Fig. 8a). Above $B = 5$ T, the lower state is not any longer the ground state (compare Fig. 5d). In the eccentric ring the oscillator strength is transferred from the ground state to higher states with increasing magnetic field (Fig. 8b) as already discussed in detail in Section III–B. Although the oscillation of the lowest bright state can be hardly seen in both cases, their second derivatives reveals them clearly (see Fig. 5f). The excited states exhibit much stronger oscillations since here the Coulomb attraction between electron and hole acts much less. Both periods agree well with Eqs. (21) and (22), respectively.

In view of an easier interpretation of the calculated spectra, we envisage in Figs. 9 and 10 a PL detection with circularly polarized light σ^+ . Thus, only the lower Zeeman splitted lines are seen. For solving the kinetic equations, nine exciton states were taken into account. First, we investigate the case without non-radiative decay, $d_{\alpha} = 0$ (Fig. 9). Due to the large energy difference between the first and the second bright state, only the lowest one is visible for both temperatures (Fig. 9a and c). The results for the eccentric ring are not so simple. Although the oscillator strength of the ground state goes down appreciably (at $B = 25$ T it is less than 10^{-2} of its value at $B = 0$ T), the luminescence line at $T = 4$ K (Fig. 9b) has almost constant intensity, and no line quenching is seen. This is a consequence of the

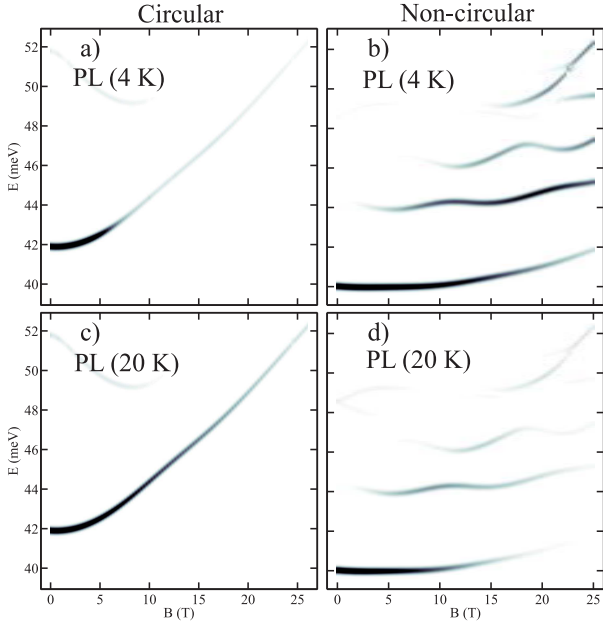


FIG. 10: Calculated photoluminescence spectra as in Fig. 9, but here with a state independent non-radiative rate of $d_\alpha = 10 \text{ ns}^{-1}$.

conservation law Eq. (29) and will be discussed below in more detail. At elevated temperature, other lines are seen as well, but their intensities have a different B dependence compared to the absorption, which signals the role of exciton occupation (Fig. 9d).

Second, non-radiative decay is included in Fig 10. For the discussion, three rates respectively times are important: (i) the radiative rate r_α (tens of nanoseconds), (ii) the exciton-phonon scattering rate $\gamma_{\alpha\beta}$ (several picoseconds), and (iii) the non-radiative rate d_α which is a phenomenological input here. With the assumption $d_\alpha = 1/(100 \text{ ps})$ we use a value which dominates over the extremely small radiative rate, but is well below the phonon scattering rate. We start again with the discussion of the circular ring where the situation is simple. Due to the change of the ground state from bright to dark one at $B > 5 \text{ T}$, these excitons decay predominantly non-radiatively, which results in a distinct line quenching (Fig. 10a and c). On the other hand, for the non-circular nanoring more lines are seen in the PL, in particular at low temperatures (Figs. 10b and d). Obviously, complete equilibration with the lattice temperature is no longer reached. For the unrealistic case of non-radiative rates being stronger than the phonon scattering, the exciton occupation is simply given by the ratio between pump rate g_α and decay d_α . Keeping both quantities constant, the exciton occupation gets constant, and the PL spectra would coincide with the absorption spectra. Although this extreme limit is not reached with the actual parameters, the tendency is clearly observable in Fig. 10.

Let us now concentrate on the integrated photolumi-

nescence I which follows from Eq. (27) as

$$I \equiv \int d\omega I(\omega) = \sum_{\alpha} r_{\alpha} N_{\alpha}. \quad (30)$$

Its relation to the pump rate P will be called photoluminescence yield Y ,

$$Y \equiv \frac{I}{P} = \frac{\sum_{\alpha} r_{\alpha} N_{\alpha}}{\sum_{\alpha} g_{\alpha}}. \quad (31)$$

Without non-radiative decay ($d_\alpha = 0$), the conservation law Eq. (29) gives immediately $Y = 1$ independent of B – each excited exciton (or in general electron–hole pair) decays into one emitted photon (full curve in Fig. 11a and b).

Things change a lot if non-radiative decay channels are included, $d_\alpha > 0$. Due to the extremely small radiative rates, these processes can even dominate the exciton decay, leading to a yield much below unity (Fig. 11c and d). Since the ground state of the concentric ring is getting dark at around $B = 5 \text{ T}$, a steep decay of the yield follows. In the eccentric nanoring the yield goes down not as abruptly since the oscillator strength of the ground state decays more slowly. The slight oscillations seen in the full curve of Fig. 11d are related to the changing level distances which influence the individual phonon scattering rates. We conclude that the quenching of the total PL is intimately related to non-radiative processes. The quenching is not as dramatic at elevated temperatures since higher exciton states contribute more and more to the total emission (not shown).

In all cases studied here, the phonon scattering rates are dominant. Therefore, it can be expected that the occupations of the different exciton states deviate not too much from equilibrium which in the present low-density case, in accordance with Eq. (26), is characterized by the Maxwell-Boltzmann (MB) distribution

$$N_{\alpha} = C \exp(-\beta E_{\alpha}) \quad (32)$$

with $\beta = 1/k_B T$. Within this approximation, the PL yield is given by

$$Y_{\text{MB}} = \frac{\sum_{\alpha} r_{\alpha} e^{-\beta E_{\alpha}}}{\sum_{\alpha} (r_{\alpha} + d_{\alpha}) e^{-\beta E_{\alpha}}} \quad (33)$$

and shown as dotted curves in Fig. 11, indeed not very much different from the full calculation. This is the right place to discuss Ref. 12 which was the first attempt to calculate the exciton PL for a nanoring. Concerning the exciton kinetics, they (i) have assumed a Maxwell-Boltzmann distribution for the excitons and (ii) normalized the integrated PL to constant exciton density $N = \sum_{\alpha} N_{\alpha}$ – and not to pump rate P – resulting in

$$Y_{\text{MBN}} = \frac{\sum_{\alpha} r_{\alpha} e^{-\beta E_{\alpha}}}{\sum_{\alpha} e^{-\beta E_{\alpha}}}. \quad (34)$$

This normalization makes a pronounced difference when non-radiative processes are absent (dashed curve in

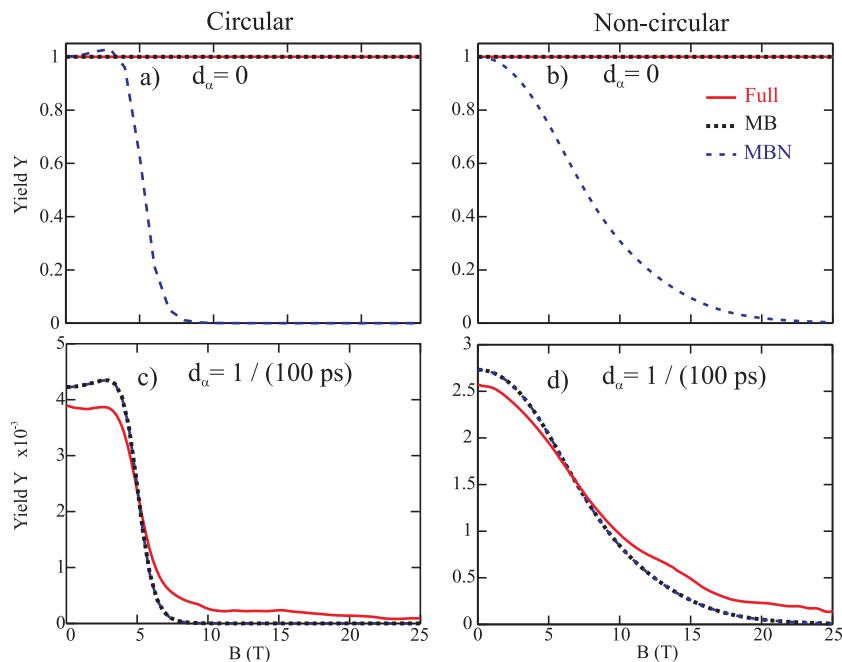


FIG. 11: (Color online) The photoluminescence yield Y for the circular (a and c) and non-circular (b and d) nanorings of Fig. 8 at $T = 4\text{K}$ and two values of the non-radiative decay rate $d_\alpha = 0$ a) and $d_\alpha = 10\text{ns}^{-1}$ b). The full solution Eq. (31) (Full, solid) is compared to the assumption of a Maxwell-Boltzmann distribution with constant pump rate Eq. (32) (MB, dotted) and with constant exciton density Eq. (34) (MBN, dashed) is plotted.

Fig. 11a), but gives nearly identical results with Eq. (33) when these dominate (dashed curve in Fig. 11b). Y_{MBN} has been normalized to Y_{MB} at $B = 0\text{T}$.

While this discussion refers to PL *quenching*, in Ref. 12 PL *blinking* was proposed, too: The integrated PL goes down and up in dependence on B , since the ground state switches between bright and almost dark behavior. The authors have used a ring model with zero width and rather close radii for electron and hole. The latter seems to be decisive for the blinking effect to occur. For the type II nanoring studied in the present work, such a blinking cannot be expected since the average electron and hole radii are rather different ($R_e = 12.1\text{nm}$ vs. $R_h = 4.4\text{nm}$). Moreover, the blinking effect predicted in Ref. 12 has been questioned recently by noting that a better account of the Coulomb interaction is needed.¹⁷

VI. CONCLUSIONS AND OUTLOOK

We have derived the Hamiltonian for excitons in nanorings with *finite width* and *arbitrary symmetry*. Sorting its matrix elements according to the symmetry point group of the confining potential we have shown how the different wave function components are coupled. Two prototype systems of type I (GaAs/AlGaAs) and type II (InP/GaInP) have been considered. The numerical investigations showed that: (i) The oscillation amplitude of the exciton Aharonov-Bohm effect decreases when going from circular to non-circular symmetry due to the addi-

tional localization of the exciton. Moreover, the oscillation period in type II nanorings changes from relative-motion induced to being determined by periodic changes of the center-of-mass wave function. (ii) The exciton ground state in the non-circular (eccentric) nanoring remains always optically active since the total angular momentum is no longer a good quantum number. However, its oscillator strength can be extremely small in type II nanorings.

Further, we have investigated the *exciton kinetics* within a model which includes acoustic phonon scattering and radiative and non-radiative decay. Our study of a *slightly* eccentric type II nanoring has revealed that the oscillations of the excited states are clearly visible and that the amplitude of the ground state oscillations is weaker than in the concentric ring. Calculating temperature dependent occupations of exciton states we could show how the appearance and disappearance of single lines in PL are related to their counterparts in absorption. The presence of non-radiative decay is decisive for the quenching of the integrated photoluminescence. If the exciton-phonon scattering dominates over all decay rates, a simplified description using a Maxwell-Boltzmann exciton distribution works reasonably well.

One unexpected finding is that a small violation of the circular symmetry improves the observability of the X-ABE since here all states are optically active, and anti-crossings periodic with B can be easily seen in the second derivative of the ground state energy. Non-radiative decay channels allow to see more lines in PL, thus improv-

ing the observability of X-ABE for excited states even at low temperatures. Therefore, a slightly asymmetric nanoring of type II seems to be the best candidate for the experimental confirmation of the exciton Aharonov-Bohm effect in linear optics, i.e. absorption or photoluminescence. From a practical point of view, an exactly circular nanoring would be rather the exception than the rule, given the uncertainties of nanostructure growth on patterned substrate, not to think of self-organized ring formation.

Quite recently, the possibility of implementing a flux qubit in small non-superconducting rings has been discussed.⁵⁰ Since a persistent current due to excitons can be initiated and controlled optically,²² it can be speculated that an exciton qubit in a nanoring can be formed whose function rests upon the exciton Aharonov-Bohm effect.

VII. ACKNOWLEDGEMENT

We acknowledge fruitful discussions with and helpful comments of L. Wendler and E. A. Muljarov. M. G. acknowledges financial support from the Graduate school Nr. 1025 of the Deutsche Forschungsgemeinschaft.

APPENDIX A: TECHNICAL DETAILS

The correlated one-particle densities are defined as conditional probabilities

$$n_{\alpha}^{(e)}(r_e, \phi_e) = \left| \Psi_{\alpha} \left(r_e, r, \phi = \phi_e - \varphi, \Phi = \frac{\phi_e + \varphi}{2} \right) \right|^2 \quad (\text{A1})$$

$$n_{\alpha}^{(h)}(r_h, \phi_h) = \left| \Psi_{\alpha} \left(r, r_h, \phi = \varphi - \phi_h, \Phi = \frac{\phi_h + \varphi}{2} \right) \right|^2 \quad (\text{A2})$$

where the coordinates of the other particle are fixed at (r, φ) . Note that this definition differs from the previous one in Ref. 22 where an additional integration over r was performed.

The averaged Coulomb potential is for convenience approximated by⁵¹

$$V_C(r_e, r_h, \phi) = -\frac{e^2}{4\pi\epsilon_0\epsilon_S} \frac{1}{b_C L_z} \operatorname{arcsinh} \left(\frac{b_C L_z}{r} \right),$$

where $r = \sqrt{r_e^2 + r_h^2 - 2r_e r_h \cos(\phi)}$, and L_z is the width of the quantum well (4 nm in our case). $b_C = 0.6$ is an ef-

fective parameter which has been fitted to give reasonable agreement with the quantum well Coulomb potential.

The phonon matrix elements are defined as⁵²

$$t_{\alpha\beta}^q = \sqrt{\frac{\hbar\omega_q}{2s^2\rho_M V}} \int \int dr_e dr_h \Phi_{\alpha}^*(r_e, r_h) \times \left(D_c \exp(i\mathbf{q}r_e) - D_v \exp(i\mathbf{q}r_h) \right) \Phi_{\beta}(r_e, r_h), \quad (\text{A3})$$

where ρ_M is the mass density, V the sample volume, and D_c (D_v) the deformation potential for electron (hole). Using the single sublevel approximation and the expansion of the wave function Eq. (5), we obtain in cylindrical coordinates for the three-dimensional momentum \mathbf{q}

$$t_{\alpha\beta}^q = \sqrt{\frac{\hbar\omega_q}{2s^2\rho_M V}} \sum_{L,L'} e^{-i(L-L')\phi_q} \times \left(S_{L,L'}^{\alpha\beta e}(q_{\parallel}) K_e(q_z) D_c - S_{L,L'}^{\alpha\beta h}(q_{\parallel}) K_h(q_z) D_v \right), \quad (\text{A4})$$

introducing the state dependent overlap functions $S_{L,L'}^{\alpha\beta e(h)}(q_{\parallel})$ and a z -dependent contribution

$$S_{L,L'}^{\alpha\beta e(h)}(q_{\parallel}) = \sum_l \int_0^{\infty} dr_e r_e dr_h r_h u_{l,L,\alpha}(r_e, r_h) \times u_{l\mp\frac{L-L'}{2},L',\beta}(r_e, r_h) J_{L-L'}(q_{\parallel} r_e(h)); \quad (\text{A5})$$

$$K_a(q_z) = \int dz v_a^2(z) e^{-iq_z z}. \quad (\text{A6})$$

$J_{L-L'}(x)$ are Bessel functions of the first kind, $v_a(z)$ is the confinement wave function in z -direction, and the symmetry $S_{L,L'}^{\alpha\beta e(h)}(q_{\parallel}) = S_{L',L}^{\beta\alpha e(h)}(q_{\parallel})$ holds. In order to get the scattering rate $\gamma_{\alpha\beta}$, the matrix element $t_{\alpha\beta}^q$ squared has to be integrated over \mathbf{q} . The integration over q_z is performed using the energy conserving delta function in Eq. 25 which gives $|\Delta_{\alpha\beta}| = \hbar s q$ with the energy difference between states $\Delta_{\alpha\beta} = E_{\alpha} - E_{\beta}$. Defining the overlap sum

$$W_{\alpha\beta}^{ab}(q_{\parallel}) = \sum_{LMN} S_{L,L-N}^{\alpha\beta a}(q_{\parallel}) S_{M,M-N}^{\alpha\beta b}(q_{\parallel}), \quad (\text{A7})$$

the final expression is obtained as

$$\gamma_{\alpha\beta} = \frac{n_B(\Delta_{\alpha\beta})\Delta_{\alpha\beta}}{2\pi\hbar^2 s^3 \rho_M} \int_0^q \frac{dq_{\parallel} q_{\parallel}}{\sqrt{1 - q_{\parallel}^2/q^2}} [W_{\alpha\beta}^{ee}(q_{\parallel})K_e^2(q_z)D_c^2 + W_{\alpha\beta}^{hh}(q_{\parallel})K_h^2(q_z)D_v^2 - 2W_{\alpha\beta}^{eh}(q_{\parallel})K_e(q_z)K_h(q_z)D_c D_v], \quad (\text{A8})$$

where $q_z = \sqrt{q^2 - q_{\parallel}^2}$. Note that both phonon emission and absorption processes (first and second term in Eq. (25), resp.) are included here, since $\Delta_{\alpha\beta}$ can have both signs.

In order to simplify further, an approximation introduced in Ref. 23 is adopted here, too. The strongest confinement is found in the growth direction z which allows to put $K_a^2(q_z) \sim K_a^2(0) = 1$. Further, a rapid decay of $W_{\alpha\beta}^{ab}(q_{\parallel})$ is assumed, well before the integration limit q is reached. Then, the integral in Eq. (A8) can be approximated by

$$\int_0^q \frac{dq_{\parallel} q_{\parallel}}{\sqrt{1 - q_{\parallel}^2/q^2}} [\dots] \approx \int_0^{\infty} dq_{\parallel} q_{\parallel} [\dots],$$

which allows to integrate over q_{\parallel} analytically using⁵³

$$\int_0^{\infty} dq_{\parallel} q_{\parallel} J_N(r_a q_{\parallel}) J_N(r_b q_{\parallel}) = \frac{1}{r_a} \delta(r_a - r_b).$$

The general expression Eq. (A8) reduces to

$$\gamma_{\alpha\beta} = \frac{n_B(\Delta_{\alpha\beta})\Delta_{\alpha\beta}}{2\pi\hbar^2 s^3 \rho_M} \times [X_{\alpha\beta}^{ee} D_c^2 + X_{\alpha\beta}^{hh} D_v^2 - 2X_{\alpha\beta}^{eh} D_c D_v], \quad (\text{A9})$$

introducing the following abbreviations:

$$\begin{aligned} X_{\alpha\beta}^{ab} &= \sum_{LMN} \int_0^{\infty} dr r \xi_{LL-N}^{\alpha\beta a}(r) \xi_{MM-N}^{\alpha\beta b}(r), \\ \xi_{LL'}^{\alpha\beta e}(r) &= \sum_l \int_0^{\infty} dr' r' u_{l,L,\alpha}(r, r') u_{l-\frac{L-L'}{2}, L', \beta}(r, r'), \\ \xi_{LL'}^{\alpha\beta h}(r) &= \sum_l \int_0^{\infty} dr' r' u_{l,L,\alpha}(r', r) u_{l+\frac{L-L'}{2}, L', \beta}(r', r). \end{aligned}$$

The detailed balance Eq. (26) can be checked in Eq. (A9) quite directly.

-
- ¹ Y. Aharonov and D. Bohm, Phys. Rev. **115**, 485 (1959).
² R. G. Chambers, Phys. Rev. Lett. **5**, 3 (1960).
³ G. Möllenstedt and W. Bayh, Naturwiss. **49**, 81 (1962).
⁴ A. Lorke, R. J. Luyken, A. O. Govorov, J. P. Kotthaus, J. M. García, and P. M. Petroff, Phys. Rev. Lett. **84**, 2223 (2000).
⁵ L. Wendler and V. M. Fomin, Phys. Rev. B **51**, 17814 (1995).
⁶ L. Wendler, V. M. Fomin, A. V. Chaplik, and A. V. Govorov, Phys. Rev. B **54**, 4794 (1996).
⁷ A. Puente, L. Serra, and R. G. Nazmitdinov, Phys. Rev. B **69**, 125315 (2004).
⁸ A. V. Chaplik, Pis'ma Zh. Eksp. Teor. Fiz. **62**, 885 (1995), [JETP Lett. **62**, 900 (1995)].
⁹ R. A. Römer and M. E. Raikh, Phys. Rev. B **62**, 7045 (2000).
¹⁰ K. Mouloupoulos and M. Constantinou, Phys. Rev. B **70**, 235327 (2004).
¹¹ D. S. Citrin and A. V. Maslov, Phys. Rev. B **72**, 073302 (2005).
¹² L. G. G. V. D. da Silva, S. E. Ulloa, and A. O. Govorov, Phys. Rev. B **70**, 155318 (2004).
¹³ L. G. G. V. D. da Silva, S. E. Ulloa, and T. V. Shahbazyan, Phys. Rev. B **72**, 125327 (2005).
¹⁴ A. V. Maslov and D. S. Citrin, Phys. Rev. B **67**, 121304(R) (2003).
¹⁵ T. Y. Zhang, W. Zhao, and J. C. Cao, Phys. Rev. B **72**, 165310 (2005).
¹⁶ A. O. Govorov, S. E. Ulloa, K. Karrai, and R. J. Warburton, Phys. Rev. B **66**, 081309(R) (2002).
¹⁷ Z. Barticevic, M. Pacheco, J. Simonin, and C. R. Proetto, Phys. Rev. B **73**, 165311 (2006).
¹⁸ H. Hu, J.-L. Zhu, D.-J. Li, and J.-J. Xiong, Phys. Rev. B **63**, 195307 (2001).
¹⁹ J. Song and S. E. Ulloa, Phys. Rev. B **63**, 125302 (2001).
²⁰ I. Galbraith, F. J. Braid, and R. J. Warburton, phys. stat. sol. (a) **190**, 781 (2002).
²¹ F. Palmero, J. Dornignac, J. C. Eilbeck, and R. A. Römer, Phys. Rev. B **72**, 075343 (2005).
²² M. Grochol, F. Grosse, and R. Zimmermann, Phys. Rev. B **74**, 115416 (2006).
²³ R. Zimmermann and E. Runge, phys. stat. sol. (a) **164**, 511 (1997).
²⁴ M. Grochol, F. Grosse, and R. Zimmermann, phys. stat. sol. (b) **243**, 3834 (2006).
²⁵ E. Ribeiro, A. O. Govorov, J. W. Carvalho, and G. Medeiros-Ribeiro, Phys. Rev. Lett. **92**, 126402 (2004).
²⁶ A. Kalameitsev, V. Kovalev, and A. Govorov, Pis'ma Zh. Eksp. Teor. Fiz. **68**, 634 (1998), [JETP Lett. **68**, 669 (1998)].
²⁷ M. P. F. de Godoy, P. F. Gomes, M. K. K. Nakaema, F. Iikawa, M. J. S. P. Brasil, R. A. Caetano, J. R. Madureira, J. R. R. Bortoleto, M. A. Cotta, and E. Ribeiro, Phys. Rev. B **73**, 033309 (2006).
²⁸ M. Grochol, F. Grosse, and R. Zimmermann, phys. stat. sol. (c) **3**, 2518 (2006).
²⁹ M. Bayer, M. Korkusiński, P. Hawrylak, T. Gutbrod, M. Michel, and A. Forchel, Phys. Rev. Lett. **90**, 186801

- (2003).
- ³⁰ M. J. Snelling, E. Blackwood, C. J. McDonagh, and R. T. Harley, *Phys. Rev. B* **45**, 3922 (1992).
- ³¹ E. Blackwood, M. J. Snelling, R. T. Harley, S. R. Andrews, and C. T. B. Foxon, *Phys. Rev. B* **50**, 14246 (1994).
- ³² G. Bastard, *Wave mechanics applied to semiconductor heterostructures* (Les editions de physique, Paris, 1992).
- ³³ H. Haug and S. W. Koch, *Quantum theory of the optical and electronic properties of semiconductors* (World Scientific, Singapore, 1994).
- ³⁴ A. Bruno-Alfonso and A. Latgé, *Phys. Rev. B* **71**, 125312 (2005).
- ³⁵ K. Siantidis, V. M. Axt, and T. Kuhn, *Phys. Rev. B* **65**, 035303 (2001).
- ³⁶ M. Tadić, F. M. Peeters, K. L. Janssens, M. Korkusiński, and P. Hawrylak, *J. Appl. Phys.* **92**, 5819 (2002).
- ³⁷ I. Vurgaftman, J. R. Meyer, and L. R. Ram-Mohan, *J. Appl. Phys.* **89**, 5815 (2001).
- ³⁸ K. L. Janssens, B. Partoens, and F. M. Peeters, *Phys. Rev. B* **64**, 155324 (2001).
- ³⁹ S. Adachi, *Physical Properties of III-V Semiconductor Compounds* (John Wiley&Sons, New York, 1992).
- ⁴⁰ A. A. Sirenko, T. Ruf, A. Kurtenbach, and K. Eberl, in *Proceedings of the 23d International Conference on the Physics of Semiconductors*, edited by M. Scheffler and R. Zimmermann (World Scientific, Singapore, 1996), p. 1385.
- ⁴¹ K. Wu and H. Simon, Tech. Rep. 41284, Lawrence Berkeley National Laboratory (1998).
- ⁴² M. Grochol, F. Grosse, and R. Zimmermann, *J. Lumin.* **112**, 208 (2005).
- ⁴³ M. Grochol, F. Grosse, and R. Zimmermann, *Phys. Rev. B* **71**, 125339 (2005).
- ⁴⁴ E. Runge, *Solid State Physics* **57**, 149 (2002), ed. by H. Ehrenreich and F. Spaepen.
- ⁴⁵ M. A. Stroschio and M. Dutta, *Phonons in nanostructures* (Cambridge University Press, Cambridge, 2001).
- ⁴⁶ F. Grosse and R. Zimmermann, cond-mat/0610404 (2006).
- ⁴⁷ D. D. Awschalom, D. Loss, and N. Samarth, *Semiconductor Spintronics and Quantum Computation* (Springer, Berlin, 2002).
- ⁴⁸ A. Steffan and R. Phillips, *phys. stat. sol. (a)* **190**, 541 (2002).
- ⁴⁹ R. Zimmermann, *phys. stat. sol. (b)* **243**, 2358 (2006).
- ⁵⁰ E. Zipper, M. Kurpas, M. Szelag, J. Dajka, and M. Szopa, *Phys. Rev. B* **74**, 125426 (2006).
- ⁵¹ R. Zimmermann, *phys. stat. sol. (b)* **135**, 681 (1986).
- ⁵² T. Takagahara, *Phys. Rev. B* **31**, 6552 (1985).
- ⁵³ M. Abramowitz and I. A. Stegun, *Handbook of Mathematical Functions* (U.S. GPO, Washington D.C., 1972).